Available online at www.sciencedirect.com

jmr&t Journal of Materials Research and Technology

journal homepage: www.elsevier.com/locate/jmrt

Precipitation behavior of the G-phase strengthened 7Ni maraging steels

Mujin Yang [a,b], *Daobin Zhang* [a], *Zhifu Yao* [b], *Zhen Ma* [b], *Junhua Luan* [c], *Cuiping Wang* [d], *Bernd Kuhn* [e], *Zengbao Jiao* [f], *Yilu Zhao* [b], *Tao Yang* [c], *Xingjun Liu* [h,g,b,*], *Shuai Wang* [a,**]

[a] *Department of Mechanical and Energy Engineering, Southern University of Science and Technology, 1088 Xueyuan Blvd, Shenzhen 518055, China*

[b] *School of Materials Science and Engineering, Harbin Institute of Technology, Shenzhen 518055, PR China*

[c] *Department of Materials Science and Engineering, City University of Hong Kong, Hong Kong, China*

[d] *College of Materials and Fujian Provincial Key Laboratory of Materials Genome, Xiamen University, Xiamen 361005, China*

[e] *Institute of Energy and Climate Research (IEK), Microstructure and Properties of Materials (IEK-2), Forschungszentrum Jülich GmbH, 52425 Jülich, Germany*

[f] *Department of Mechanical Engineering, The Hong Kong Polytechnic University, Hong Kong, China*

[g] *Institute of Materials Genome and Big Data, Harbin Institute of Technology, Shenzhen 518055, PR China*

[h] *State Key Laboratory of Advanced Welding and Joining, Harbin Institute of Technology, Shenzhen 518055, PR China*

ARTICLE INFO

Article history:
Received 24 July 2023
Accepted 22 September 2023
Available online 26 September 2023

Keywords:
Alloy design
$Ni_{16}X_6Si_7$ G-phase
Precipitation hardening
Maraging steel
Microstructural control

ABSTRACT

In this study, G-phase strengthened 7Ni maraging alloys were studied using a combination of thermodynamic prediction based on the TCFE-7 database and advanced experimental techniques, including micro-hardness testing, electron backscatter diffraction (EBSD), in-situ X-ray diffraction (XRD), transmission electron microscopy (TEM), and atom probe tomography (APT). The martensite reversion and phase stability of overcooled austenite were precisely determined for a series of Fe–7Ni–2Si-based alloys, validating the effectiveness of thermodynamic predictions in martensite transformation.

Based on these theoretical prediction, aging hardness measurements and microstructural observations further revealed that $Ni_{16}X_6Si_7$-G (X = Ti, Nb, Ta) precipitates are effective strengthening phases in 7Ni maraging steel, with the exception of $Ni_{16}X_6Si_7$ (X = Mn, Zr) due to their significantly different thermal stabilities. Experimental results showed that the $Ni_{16}X_6Si_7$-G (X = Ti, Nb, Ta) precipitates remained stable and densely distributed within the martensitic matrix after aging at 500 °C, resulting in high aging hardness values ranging from 350 to 550 HV. Among the studied alloys, the 1Ti alloy strengthened by the $Ni_{16}Ti_6Si_7$-G phase exhibited the finest particle radius (estimated at 1.4 nm) and the highest number density (estimated at $1.9 \times 10^{24}/m^3$). Additionally, it is worth noting that the $Ni_{16}Zr_6Si_7$-G phase was believed to form through eutectic reaction with α-Fe during solidification and the $Ni_{16}Mn_6Si_7$-G phase was only stable at temperatures below 460 °C and was not detected experimentally.

* Corresponding author. State Key Laboratory of Advanced Welding and Joining, Harbin Institute of Technology, Shenzhen 518055, PR China.
** Corresponding author.
E-mail addresses: xjliu@hit.edu.cn (X. Liu), wangs@sustech.edu.cn (S. Wang).

https://doi.org/10.1016/j.jmrt.2023.09.230

These findings enhance our comprehension of G-phase precipitation and strengthening in 7Ni maraging steel and underscore the potential for utilizing thermodynamic calculations and advanced experimental techniques to guide the design and optimization of high-strength alloys.

1. Introduction

Nano-precipitation strengthening has gained significant importance in the enhancement of mechanical properties of various maraging steels. This method involves the formation of super-fine precipitates with an extremely high number density (>10^{23} m^{-3}) [1–12]. For instance, the inclusion of the ordered B2–NiAl phase in an 18Ni maraging steel has led to precipitation strengthening, resulting in an impressive yield strength of ~2.2 GPa and a notable elongation of ~8% [1]. A recent breakthrough in this field pertains to the simultaneous precipitation of Ni_3Mo and Mo-rich nanoprecipitates, which has resulted in the emergence of a novel category of ultra-high-strength steel boasting an impressive grade of 2.5 GPa [11]. Furthermore, extensive research is being conducted on various other nano-precipitates, such as Cu-rich phases [13–15], κ-carbide [16–18], $L2_1$-Ni_2TiAl phase [7,19–25] among others, in the field of structural materials.

The G-phase, a ternary silicide with a chemical formula of $A_{16}M_6Si_7$ (A = Fe, Ni, Co; M = transition elements) [26–30], is also a commonly observed precipitate in various Fe-based alloys [31–36]. However, its potential as a strengthening phase has received limited attention. Schulz-Beeken and Hougardy (SBH) [37] were the first to deliberately utilize the G-phase as a strengthening precipitate in a Fe–2Si–1Ti–4Mn–3Ni–1Cr (wt. %) martensitic alloy. Subsequently, the G-phase was discovered in a Co-free high Cr maraging steel, and its characteristics were carefully examined by several researchers [38]. Recently, Sun et al. [7] reported a novel Fe–Ni–Si–Ti maraging steel with a high number density of nanoscale G-phase precipitates, exhibiting exceptional super-high strength. Furthermore, G-phase has been also identified as finely dispersed precipitates within the ferrite phase of duplex steels following extended service periods at temperatures ranging from 300 °C to 600 °C [39–43]. In all of these studies, a noteworthy common observation is the strict cube-on-cube orientation relationship maintained between the G-phase and the matrix, highlighting its significant potential as a strengthening phase.

Despite the existence of multiple variants of G-phase as indicated by experimental phase diagrams (which suggest the presence of up to 17 variants), only a limited number of G-phases have been discovered and effectively utilized in steels. Moreover, there is a significant lack of systematic research and comparison among different G-phase variants, particularly regarding their potential as strengtheners in Fe-based alloys. To address this gap, we have dedicated our efforts to exploring a series of maraging alloys that incorporate various G-phase species predicted by thermodynamic database. The primary objective of this research is to investigate the precipitation behavior of Fe–7Ni maraging alloys featuring different G-phase variants. Our aim is to comprehensively examine their precipitation behaviors, with a particular emphasis on contrasting their distinct thermal stabilities and precipitation strengthening effects. Through these meticulous analyses, our intention is to uncover valuable insights into the potential of various G-phase variants as strengthening phase in Fe-based alloys.

2. Alloy design

To conduct our study, we utilized a series of high-purity metals (>99.9%) including Iron (Fe), Nickel (Ni), Silicon (Si), Titanium (Ti), Niobium (Nb), Tantalum (Ta), Zirconium (Zr), and Manganese (Mn) as raw materials. The nominal compositions of the five alloy compositions are presented in Table 1. For ease of reference, these alloys were designated as 1Ti, 1Nb, 1Ta, 1Zr, and 1Mn, respectively.

The composition of each alloy was determined based on the thermodynamic description of different G-phase species present in the TCFE-7 (V 3.0) thermodynamic database, as illustrated in Fig. 1. The calculated phase fraction versus temperature diagrams for the 1Ti, 1Nb, 1Zr, and 1Mn alloys are depicted in Fig. 1a, b, 1c and 1 d, respectively. From these diagrams, it is evident that the main or matrix phases in these compositions are austenite (depicted in red) and ferrite (depicted in blue). At elevated temperatures, austenite predominates, whereas the ferrite phase dominates in the low-temperature region. The phase transformation from austenite to ferrite occurs at ~800 °C.

Regarding precipitates, both G-phase (depicted in brown) and Laves phase (depicted in purple) appear simultaneously in the 1Ti, 1Nb, and 1Zr alloys, while only G-phase is observed in the 1Mn alloy. The phase fractions of G-phase and Laves phase do not exceed 5 wt % in these alloys. The dissolution temperature of G-phase follows the ranking: 1Zr (840 °C) > 1Nb (710 °C) > 1Ti (650 °C) > 1Mn (460 °C). The temperature ranges for the appearance of Laves phase are 640 °C–960 °C for 1Ti,

Table 1 – Nominal compositions of the studied alloys in this work (wt.%).

Label	Fe	Ni	Si	X (G-former)
1Ti	90	7	2	1 Ti
1Nb	90	7	2	1 Nb
1Ta	90	7	2	1 Ta
1Zr	90	7	2	1 Zr
1Mn	90	7	2	1 Mn

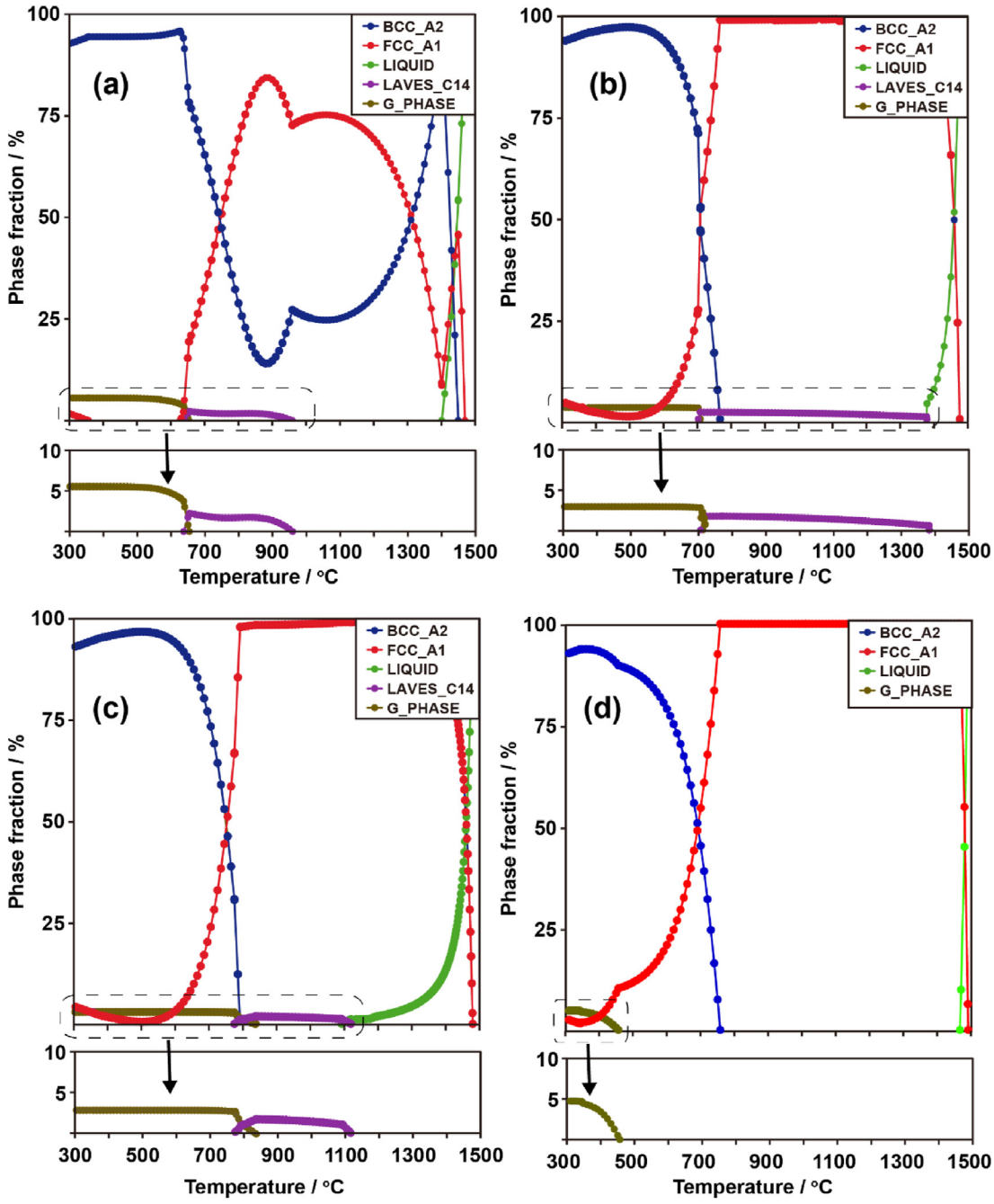

Fig. 1 – Phase fraction versus temperature diagrams calculated using the Fe-based alloy thermodynamic database for the following alloys: (a) 1Ti, (b) 1Nb, (c) 1Zr, and (d) 1Mn.

700 °C–1390 °C for 1Nb, and 780 °C–1120 °C for 1Zr. These thermodynamic calculations presented in Fig. 1 indicate that the alloying elements Ti, Nb, Zr, and Mn promote the precipitation of G-phase in the alloys.

In light of our recent experimental phase diagram study [44,45], it has been observed that elemental Tantalum (Ta) exhibits characteristics similar to Niobium (Nb) as a strong G-phase-forming element. Consequently, the 1Ta alloy was prepared to validate this hypothesis, without relying on thermodynamic calculations. While it has been acknowledged that some adjustments to the thermodynamics of this system are necessary based on previous research [7], utilizing the existing thermodynamic calculations still serves as a reasonable starting point for alloy development, as we will demonstrate.

3. Experimental procedure

The ingots were prepared by arc-melting under an argon (Ar) atmosphere and subsequently drop cast into a copper mold. Following this, the ingots underwent a homogenization process at 1200 °C for 1 h. Afterward, cold rolling treatment was applied, resulting in a total deformation rate of ~80%. The cold-rolled sheets were eventually reduced to a thickness of

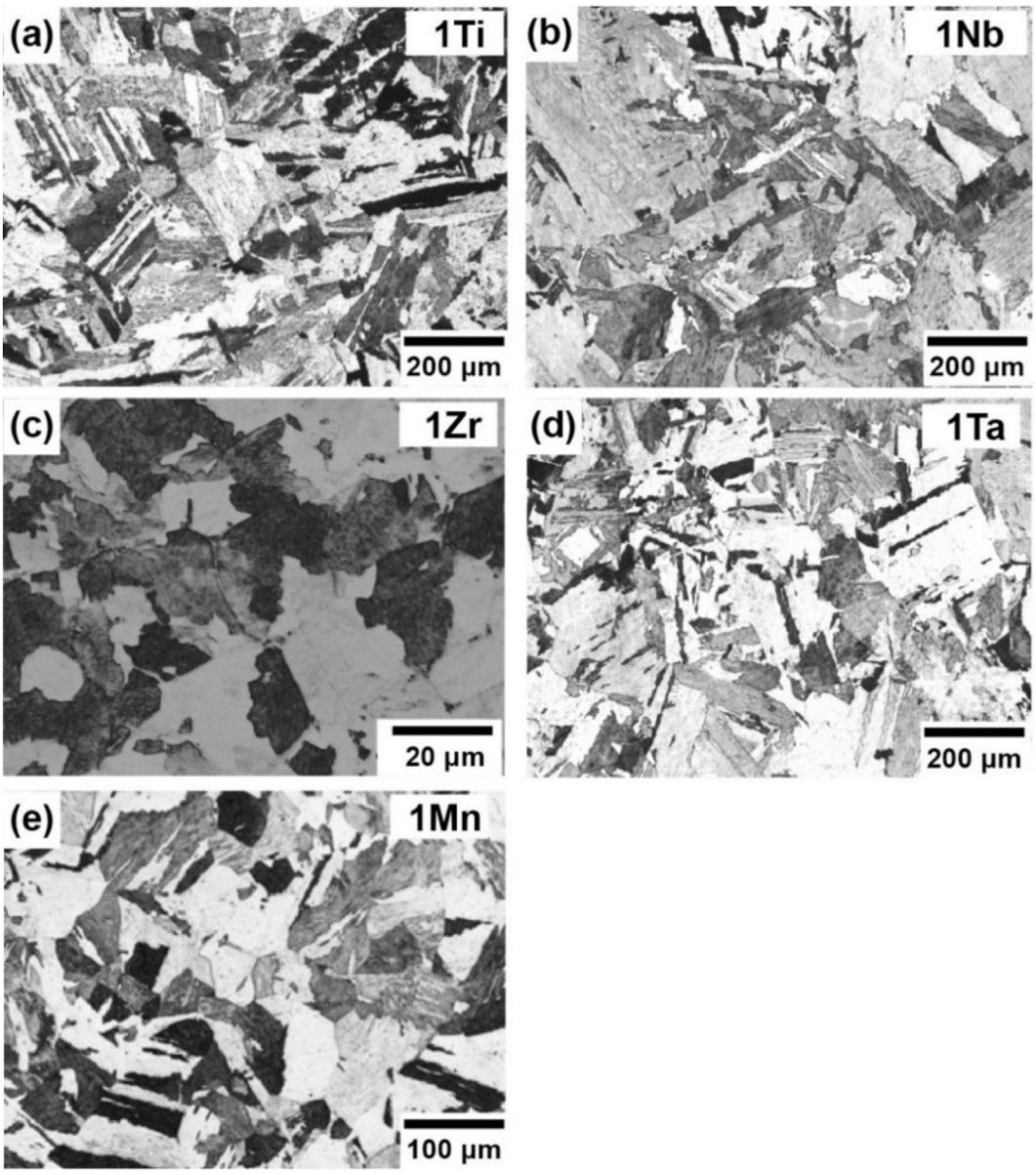

Fig. 2 – Optical micrographs of the 1Ti, 1Nb, 1Zr, 1Ta, and 1Mn alloys after quenching from 1000 °C following a 20-min annealing treatment.

1 mm (from an initial thickness of 5 mm). Following the cold rolling process, the sheets underwent a solution treatment at 1000 °C for 20 min to achieve a martensite microstructure. Specimens for heat treatment, microstructural observation, and micro-hardness analysis were obtained by cutting sections from these cold-rolled sheets. The specimens were then cold-mounted using epoxy resin, followed by polishing with a suspended diamond polishing solution until a finished surface with a 1 μm roughness was achieved. Micro-hardness analysis was conducted using a Shimadzu Micro-Hardness Tester with a 4.9 N load and a 15-s holding time. Each sample underwent seven tests, and the average values of the measured data were recorded. Tensile samples, with a gauge length of 10 mm and a width of 3 mm, were also prepared by cutting them from the cold-rolled sheets, in alignment with the rolling direction.

Optical microscopy (OM) was employed to observe the martensitic microstructure after etching with a 10% nital solution. For microstructural observation and phase composition analysis, high-resolution field emission scanning electron microscopy (HR-FESEM) was utilized, specifically the Zeiss Merlin SEM with energy-dispersive X-ray spectroscopy (EDX) capability. Crystal structure identification of the martensitic matrix and precipitates was performed using electron backscattered diffraction (EBSD) analysis. To determine the stability of undercooled austenite and martensite reversion transformation temperatures, temperature variable in-situ X-ray diffraction (XRD) was employed. The heating and cooling rate during the XRD measurements was set at 5 K/min, ranging from room temperature (RT) to 850 °C. At each 25 °C interval, the temperature was held for 15 min to allow for

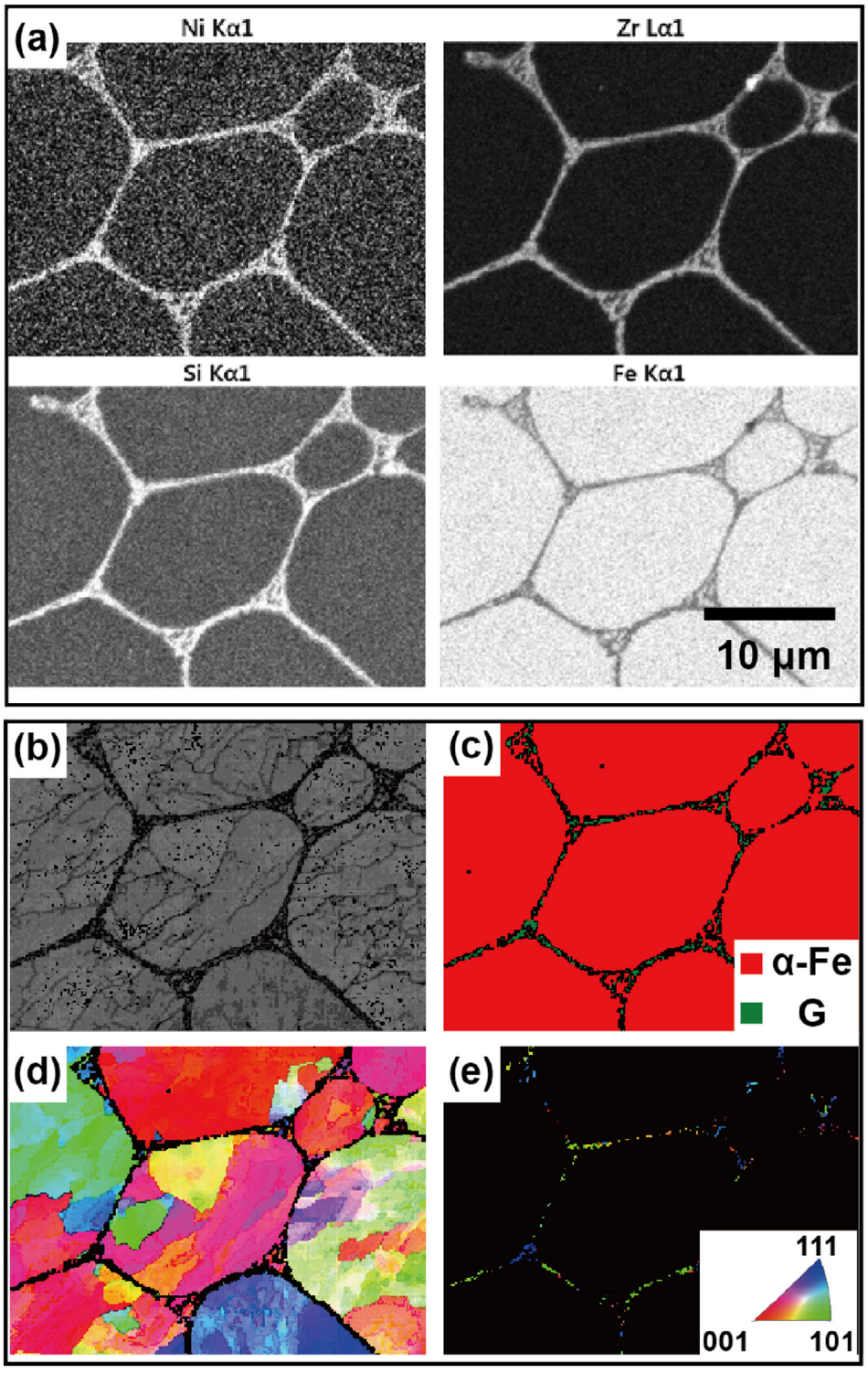

Fig. 3 – EDS elemental mapping and EBSD analysis of the 1Zr alloy after quenching from 1000 °C: (a) Elemental distribution of Ni, Zr, Si, and Fe; (b) Band contrast map; (c) Phase distribution map; (d) and (e) Inverse pole figure (IPF) maps.

thermal equilibration, followed by a 45-min acquisition of XRD data. This process enabled the detection of the phase transformation between austenite and ferrite phases.

To prepare transmission electron microscopy (TEM) foils, 2 mm thick slices were obtained from the aged-treated specimen using an electro discharge cutting machine. These slices were then ground down to a thickness of 100 μm. Subsequently, 3 mm diameter discs were punched out from the ground slices. The discs underwent jet electro-polishing in a 10 vol % $HClO_4$ ethanol solution to achieve a thin and electron-

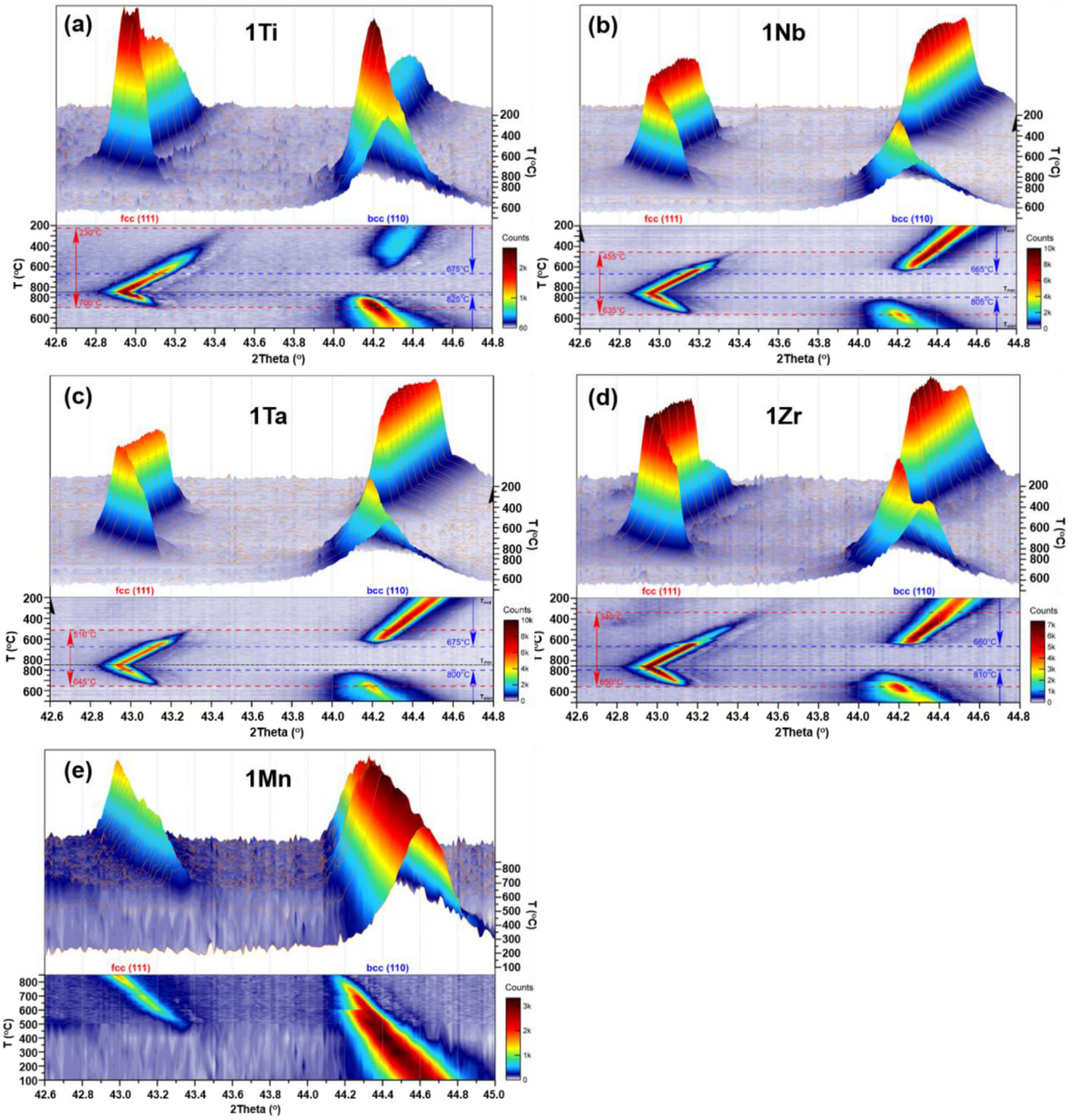

Fig. 4 – Variable-temperature in-situ X-ray diffraction patterns of quenched alloys: (a) 1Ti, (b) 1Nb, (c) 1Ta, (d) 1Zr and (e) 1Mn.

transparent foil suitable for TEM analysis. TEM characterization was performed using a JEM 2100 transmission electron microscope operating at an acceleration voltage of 200 kV. This instrument allowed for high-resolution imaging and analysis of the microstructure and features of the foils.

For atom probe tomography (APT) analysis, needle-shaped specimens were prepared using annular milling in an FEI Scios focused ion beam/scanning electron microscope (FIB/SEM) following a conventional lift-out method [46]. This technique allowed for precise extraction of a small needle-shaped sample suitable for APT analysis. APT characterizations were carried out using a CAMECA Instruments LEAP 5000XR local electrode atom probe. The specimens were analyzed in voltage mode, with a specimen temperature maintained at 50 K. The pulse repetition rate was set to 200 kHz, and the pulse fraction was 0.2. An evaporation detection rate of 0.5% atom per pulse was utilized to capture the evaporated atoms during the analysis process. For data analysis and building three-dimensional reconstructions, Interactive Visualization and Analysis Software (IVAS™) in Versions 3.8 was employed.

This software facilitated the visualization and analysis of the acquired APT data.

4. Results

4.1. *Martensitic transformation and reversion*

Fig. 2 illustrates a series of representative optical microstructures obtained from the 1Ti, 1Nb, 1Ta, 1Zr, and 1Mn alloys. These microstructures were obtained by ice-water quenching from 1000 °C following a 20-min annealing treatment. With the exception of the 1Zr alloy (Fig. 2c), the other four alloys (1Ti, 1Nb, 1Ta, and 1Mn) exhibit a typical lath martensite morphology. This suggests that the designed Fe–7Ni–2Si-1X quaternary system possesses a strong propensity for martensite formation. In the case of the quenched 1Zr alloy, it primarily consists of polygonal block structures with varying contrasts (as seen in Fig. 2c). Additionally, a thin strip microstructure is faintly visible along the grain boundaries.

The crystal structure of the quenched 1Zr alloy was further confirmed through combined EDS-Mapping and EBSD analysis, as depicted in Fig. 3. The elemental distribution maps (Fig. 3a) illustrate a network microstructure at the grain boundary. This network grain boundary exhibits higher concentrations of Ni, Si, and Zr (appearing brighter) and lower concentrations of Fe (appearing darker). This strongly suggests the presence of a Ni–Si–Zr-type G-phase along the grain boundary, forming a cell microstructure. The band contrast map in Fig. 3b reveals numerous sub-grains within the cell, indicating the presence of martensite. EBSD analysis employing Kikuchi-line indexing (Fig. 3c, d and 3e) further confirms the aforementioned observation. The phase distribution maps in Fig. 3c indicate that the cell region (highlighted in red) corresponds to bcc-Fe, while the network structure (highlighted in green) represents the $Ni_{16}Zr_6Si_7$_G phase. The corresponding inverse pole figure (IPF) maps in Fig. 3d and **e** exhibit no noticeable texture within the martensite cell and G-phase network.

Fig. 4 illustrates the X-ray diffraction patterns obtained from the 1Ti, 1Nb, 1Ta, 1Zr, and 1Mn alloys during the heating and cooling cycles within the temperature range of 500 °C–850 °C. In order to facilitate comprehension, only the diffraction peaks within the range of 42°–45° were selected and displayed, as they encompass the significant peaks of bcc (110) and fcc (111). The heating process from 500 °C to 850 °C reveals a noticeable trend: the intensity of the bcc (110) peak gradually diminishes. Concurrently, the fcc (111) peak emerges at a specific temperature and exhibits increased intensity with further temperature elevation. This observed behavior can be attributed to the occurrence of martensite reversion (b.c.c → f. c.c) phase transformation. During the cooling process, the transformations observed reflect the stability of the overcooled austenite phase. To facilitate comparison and reference, the specific temperatures associated with these transformations are accurately pinpointed in Fig. 4.

The X-ray diffraction pattern of the 1Mn alloy (Fig. 4e) reveals an unexpected phase stability of ferrite (b.c.c lattice) beyond 850 °C, making it the highest among all the alloys investigated. This finding is significant when considering the 1000°C-quenched microstructure (Fig. 2e). The conclusion can be drawn that the ferrite phase in the 1Mn alloy should disappear between 850 °C and 1000 °C. In contrast, the ferrite phase in the other four alloys (1Ti, 1Nb, 1Zr, and 1Ta) exhibits disappearance temperatures ranging from 800 °C to 825 °C. These results suggest that the microstructure of these alloys can be tailored into two distinct types by controlling the quenching temperature. One type corresponds to a microstructure consisting solely of martensite, which is the main focus of this article. The other type is characterized by a duplex structure composed of 'martensite plus ferrite'.

4.2. *Precipitation hardening*

Fig. 5 presents the aging hardening curves obtained at 500 °C for the 1Ti, 1Nb, 1Ta, and 1Mn alloys subsequent to quenching from 1000 °C. The 1Zr alloy was excluded from further aging treatment due to the confirmed occurrence of the expected $Ni_{16}Zr_6Si_7$_G strengthening phase at grain boundaries in the quenched state (Fig. 3). The results demonstrate a clear variation in the aging hardening behavior among the alloys. Notably, the 1Ti specimen exhibits the most significant aging hardening effect, followed by the 1Nb alloy, while the 1Ta alloy displays the weakest response. The peak hardness for the 1Ti specimen reaches a remarkable value of 550 HV at 2 h of aging. Conversely, the 1Nb alloy attains a peak hardness of around 450 HV after approximately 4 h of aging. In the case of the 1Ta alloy, the micro-hardness progressively increases with increasing aging time but fails to reach a peak within the 24-h aging period. Unfortunately, the 1Mn alloy does not demonstrate any significant increase in micro-hardness throughout the aging process.

These findings emphasize the distinctive aging hardening behaviors observed in the investigated alloys, with the 1Ti alloy exhibiting the most prominent strengthening effect, followed by the 1Nb alloy, while the 1Ta and 1Mn alloys demonstrate comparatively weaker responses. Consequently, the aged-treated 1Ti, 1Nb, and 1Ta specimens were subjected

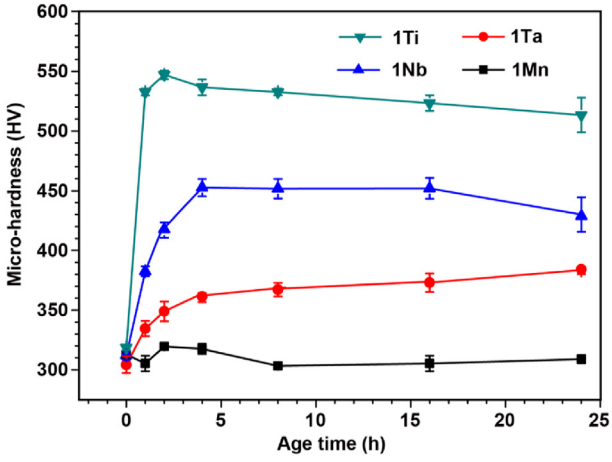

Fig. 5 – The aging hardening curves at 500 °C for the quenched 1Ti, 1Nb, 1Ta and 1Mn alloys.

to further transmission electron microscopy (TEM) analysis to elucidate the nature of the precipitates. The results of this analysis are presented in Figs. 6–9.

Fig. 6 presents the nanosized precipitates observed in the 500 °C/12h-aged 1Ti specimen. Two thin areas with different incident directions, namely the $100_{b.c.c}$ (Fig. 6a and b) and $111_{b.c.c}$ (Fig. 6c–g), were examined to analyze the crystal structure of the precipitates. In the bright field micrographs of Fig. 6a and c, the morphology of the nano-precipitates within the martensitic lath is not clearly visible using either the [100] or [111] direction. This is likely due to the extremely small size of the particles. However, the double electron diffraction patterns shown in Fig. 6b and **d** indicate the presence of two distinct structures. Further pattern indexing results reveal

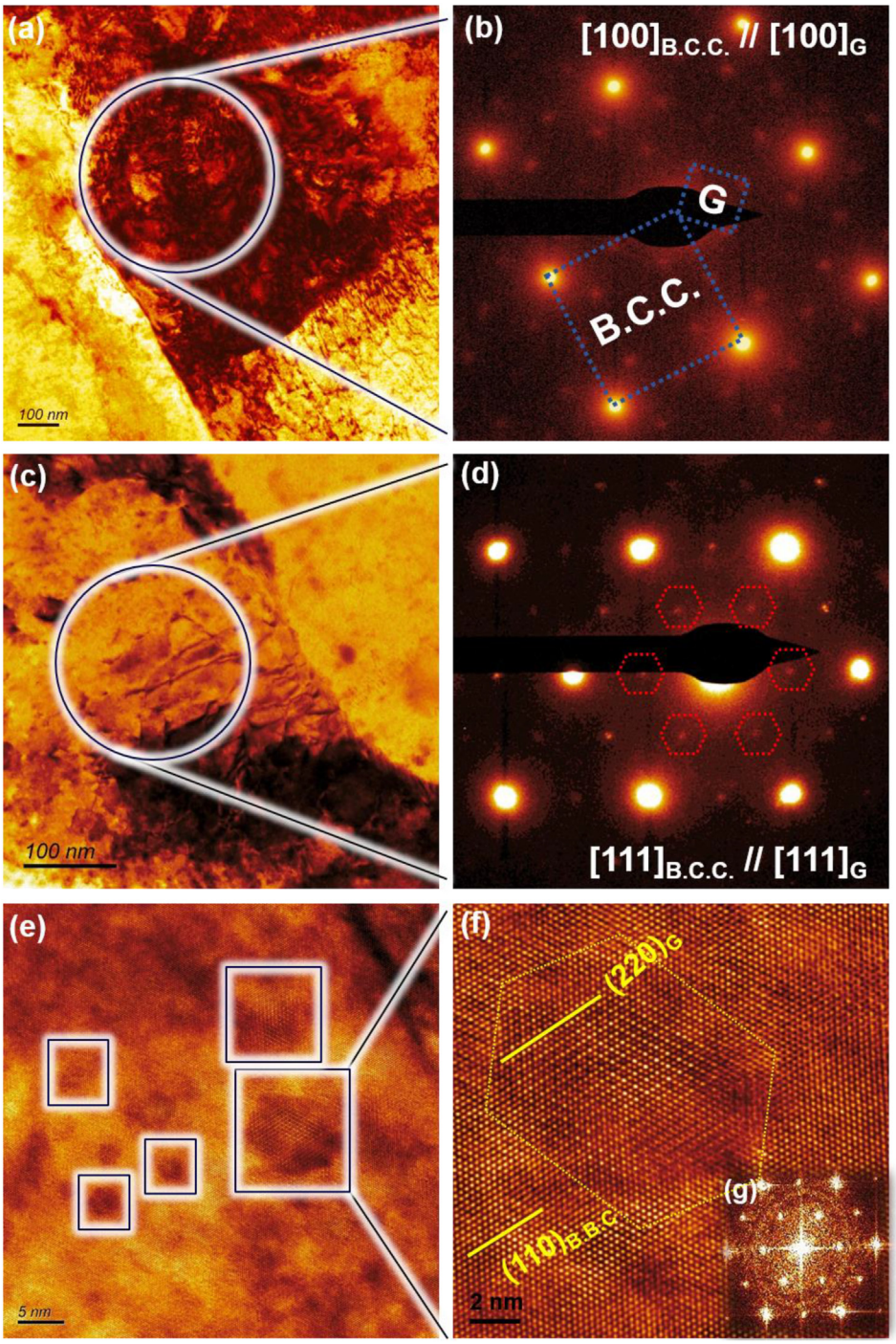

Fig. 6 – TEM characterization results of the 500 °C/12h-aged 1Ti specimen. (a) and (c): Bright field (BF) micrographs showing the martensitic matrix. (b) and (d): Selected area diffraction patterns (SAED) obtained from the regions depicted in (a) and (c), respectively. (e) and (f): High-resolution micrographs illustrating the G-phase precipitates. The inset (g) displays the fast Fourier transform (FFT) patterns derived from (f).

that the precipitate (p.p.t) and martensitic matrix (b.c.c) exhibit a cube-on-cube orientation relationship as follows: $[100]_{p.p.t}//[100]_{b.c.c}$, $[111]_{p.p.t}//[111]_{b.c.c}$, $(020)_{b.c.c}//(080)_{p.p.t}$, and $(220)_{b.c.c}//(440)_{p.p.t}$. This indicates that the lattice parameter of the precipitates is exactly four times that of the martensitic matrix. Notably, this specific orientation relationship has been widely reported in various alloys strengthened by G-phase, particularly in the presence of the $Ni_{16}Ti_6Si_7$_G phase. Therefore, it strongly suggests the existence of $Ni_{16}Ti_6Si_7$_G phase precipitates in the 1Ti alloy.

Fig. 6e presents the high-resolution micrographs of the $Ni_{16}Ti_6Si_7$_G particles obtained from the $111_{b.c.c}$ incident direction. The G-phase precipitates exhibit an average diameter of less than ~6 nm. In Fig. 6f, individual larger particles display a distinctive hexagonal feature along the face-centered cubic structure in the <111> direction. This confirms the crystallographic orientation of the G-phase particles. The inset in Fig. 6g shows the fast Fourier transform (FFT) pattern, which further confirms the strict cube-on-cube relationship between the martensitic matrix and the G-phase precipitates. The presence of a significant number of superfine G-phase precipitates (Fig. 6) may account for the notable aging hardening observed in the 1Ti alloy (Fig. 5).

Fig. 7 illustrates the transmission electron microscopy (TEM) characterization results of the 1Nb specimen, which underwent aging at 500 °C for 12 h. In the low magnification bright field micrograph displayed in Fig. 7a, numerous faintly visible spot-like particles are observed within the interior as well as at the lath boundaries. For further investigation, two representative regions, namely region b (lath interior) and region c (lath grain boundary), were chosen for detailed characterization and amplification. Upon close examination of the lath interior, as depicted in the high-resolution micrograph in Fig. 7b, densely packed superfine nano-precipitates (<5 nm in diameter) are discernible and highlighted by red circles. It is noteworthy that these nano-precipitates have been identified to belong to the characteristic G-phase, as confirmed by the inset Fast Fourier Transform (FFT) pattern. Moreover, the G-phase identified in this study is specifically denoted as $Ni_{16}Nb_6Si_7$_G. Significantly, the $Ni_{16}Nb_6Si_7$_G phase exhibits a favorable Cube-on-Cube orientation relationship with the martensitic matrix, as evidenced by the crystallographic

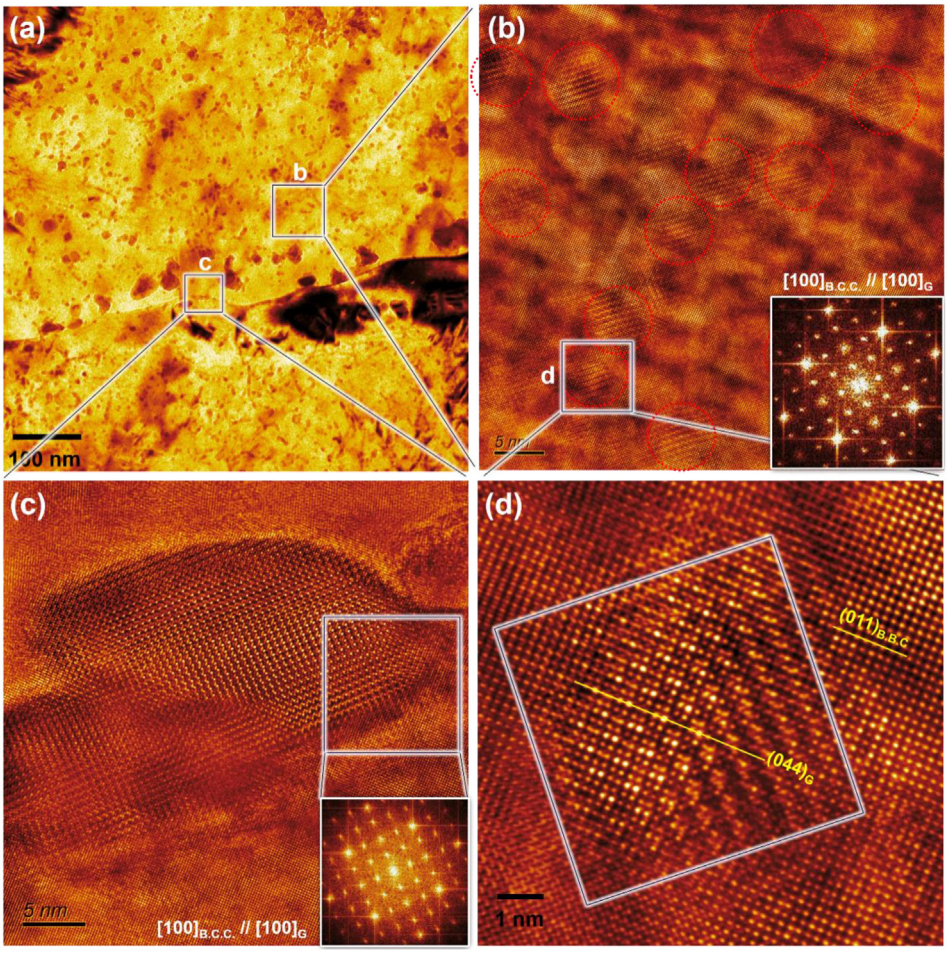

Fig. 7 – TEM characterization results of the 500 °C/12h-aged 1Nb specimen. (a) Low magnification micrograph displaying the presence of dense precipitates; (b) and (c) High-resolution micrographs showcasing the nanoscale precipitates within the lath structure and at the grain boundary, respectively; (d) Enlarged micrograph highlighting a single precipitate and its interface with the lath matrix.

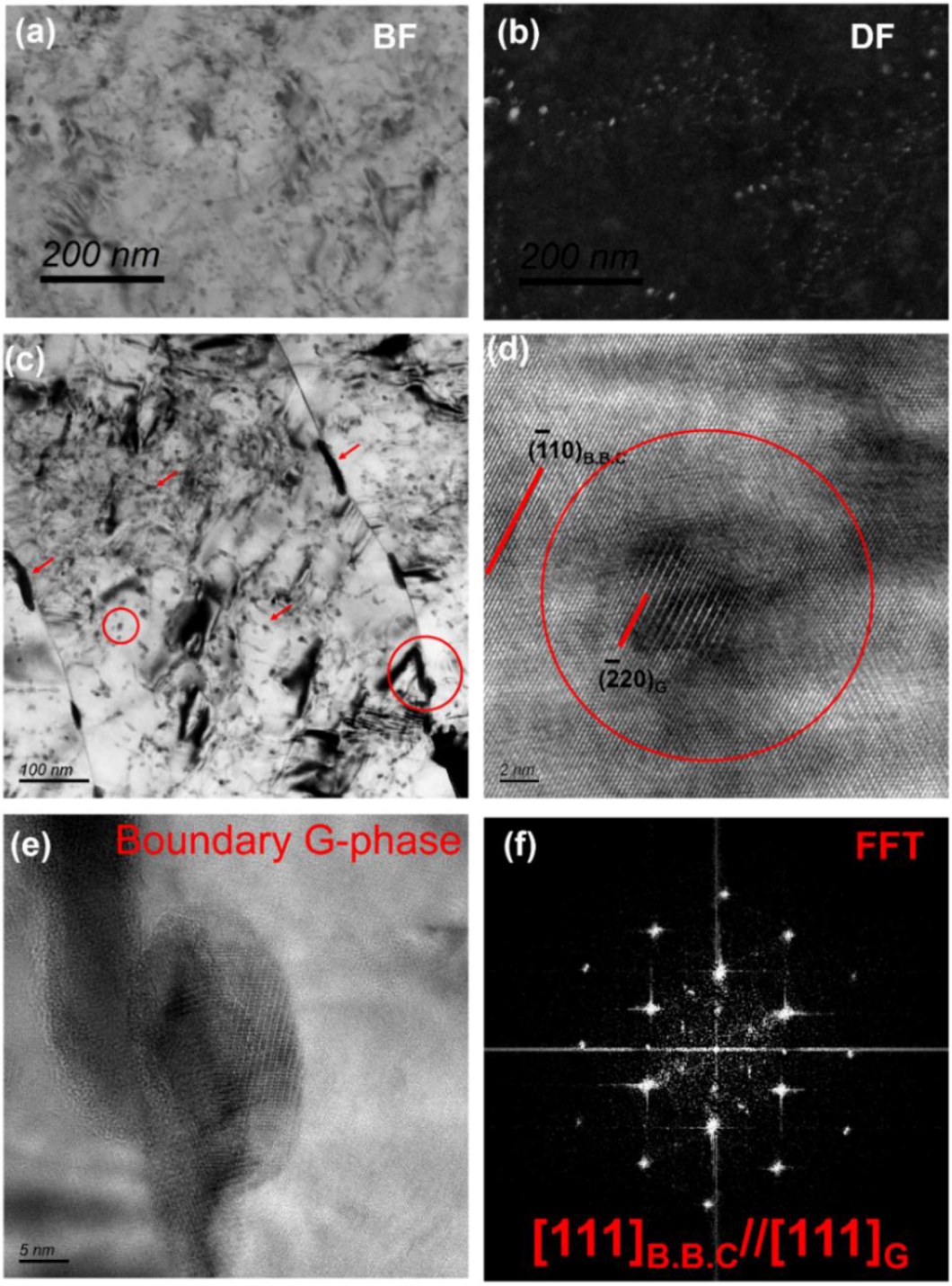

Fig. 8 – TEM and HRTEM analysis of the 500 °C/12h-aged 1Ta alloy. (a) Bright field image; (b) Dark field image; (c) Low magnification graph; (d) and (e) Partially enlarged micrographs from (c); (f) Fast Fourier Transform (FFT) pattern from (d).

alignment observed. This finding parallels the observations made for the 1Ti alloy in Fig. 6. Consequently, the formation of these $Ni_{16}Nb_6Si_7$_G precipitates is deemed to be the primary factor responsible for the considerable age-hardening observed in the 1Nb alloy.

The high-resolution micrographs presented in Fig. 7c and d provide detailed views of the interfacial arrangements between the precipitates and the adjacent matrix, specifically focusing on the grain interior and grain boundary, respectively. In Fig. 7c, the inset Fast Fourier Transform (FFT) pattern confirms that the precipitates found at the grain boundaries exhibit the same G-phase characteristics as the intragranular particles observed earlier. Notably, the G-phase particles located at the grain boundaries are considerably larger in size

compared to those within the grain. This discrepancy in size can be attributed to the higher interfacial energy present at the interlath regions. It is reasonable to expect larger particles at the grain boundaries due to the more favorable thermodynamics associated with reducing the interfacial energy. Interestingly, the interfacial arrangements between the G-phase precipitates and the adjacent matrix exhibit no discernible differences between the grain interior and the grain boundary. The same orientation relationship is maintained in both cases. However, at the lath interface, the G-phase precipitates can only maintain this specific orientation relationship with one of the two adjacent laths. This limitation arises from the inherent difference in orientation between the neighboring laths.

Fig. 8 depicts a series of TEM results obtained from the 1Ta specimen aged at 500 °C for 12 h. The bright field (BF) and corresponding dark field (DF) images presented in Fig. 8a and b, respectively, exhibit only a few particles within the lath structure. In Fig. 8c, A low-magnification image of a single lath matrix is displayed. In contrast to the 1Ti (Fig. 6a and b) and 1Nb (Fig. 7a) specimens, the 1Ta specimen (Fig, 8c) clearly reveals the presence of nanoparticles, and the spacing between these particles appears to be larger. This is believed to be the primary reason for the relatively weak age-hardening observed in the 1Ta alloy, as shown in Fig. 5. Moving to higher resolution, Fig. 8d illustrates the high-resolution microstructure of a single $Ni_{16}Ta_6Si_7$_G phase precipitate. The corresponding Fourier transform pattern is displayed in Fig. 8f, demonstrating the ubiquitous Cube-on-Cube orientation relationship between the G-phase precipitate and the martensitic matrix. Similarly to the 1Nb specimen (Fig. 8e), the presence of G-phase precipitates at the lath interfaces is also detected in the 1Ta alloy, as shown in Fig. 8e.

The 1Ti and 1Nb specimens aged at 500 °C for 12 h were further examined using atom probe tomography (APT), as illustrated in Fig. 9. However, the 1Ta alloy was not included in the analysis due to the large particle spacing observed in the $Ni_{16}Ta_6Si_7$_G phase (Fig. 8). Fig. 9 presents elemental distribution and iso-surface mapping, clearly showcasing the Ni–Ti–Si-rich (Fig. 9a) and Ni–Nb–Si-rich (Fig. 9b) variants of the G-phase. Comparing with Fig. 9a and b, it is evident that the $Ni_{16}Ti_6Si_7$_G phase exhibits a higher number density compared to $Ni_{16}Nb_6Si_7$_G.

Statistical analysis reveals that the $Ni_{16}Ti_6Si_7$_G phase has a number density of approximately 1.9×10^{24} m^{-3}, an average particle radius of 1.4 ± 0.7 nm, and a volume fraction of 1.15 vol %. In contrast, the $Ni_{16}Nb_6Si_7$_G phase exhibited an average radius of 2.0 ± 0.6 nm, a number density of 4.9×10^{23} m^{-3}, and a volume fraction of approximately 1.23 vol %. A quantitative comparison was conducted to analyze the composition, radius,

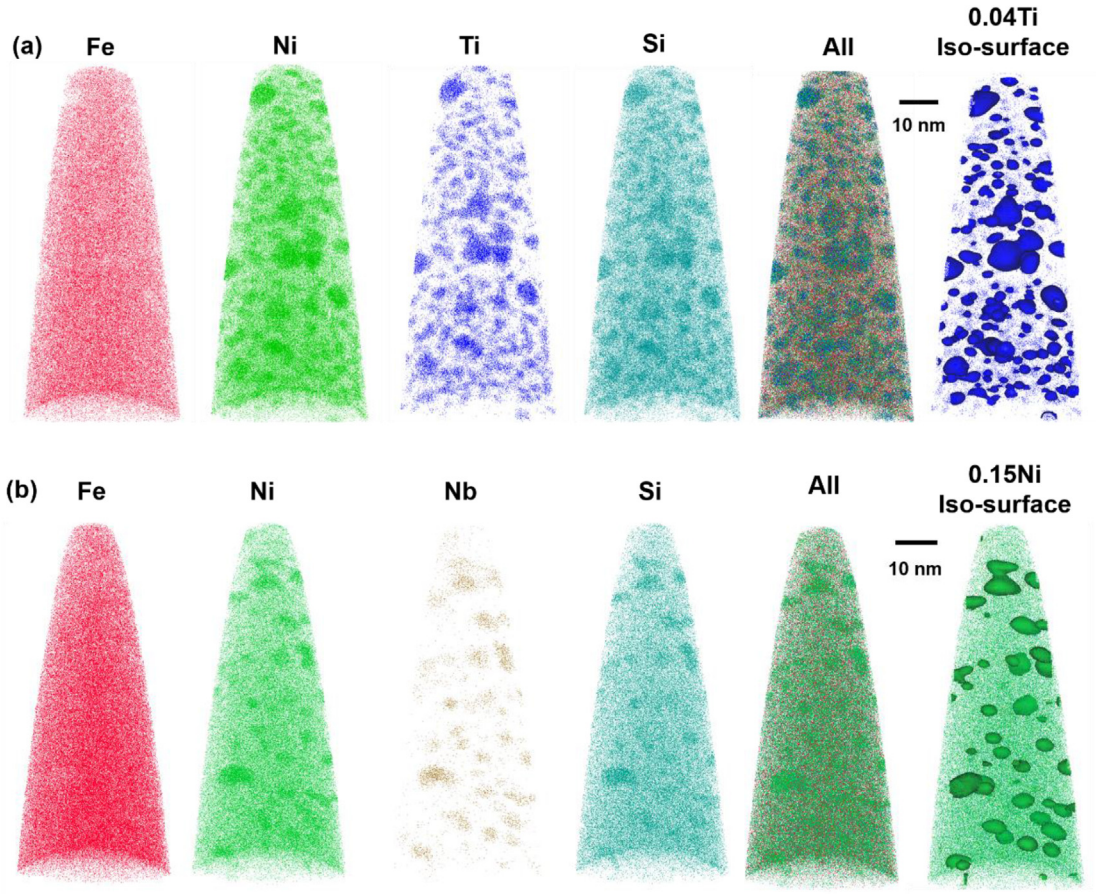

Fig. 9 – Elements distribution and iso-surface mapping of the atom probe tomography (APT) reconstruction for two 500 °C /12h-aged specimens: (a) 1Ti; (b) 1Nb.

volume fraction, and number density of the $Ni_{16}Ti_6Si_7$- and $Ni_{16}Nb_6Si_7$-G precipitates, which are illustrated in Fig. 10.

In Fig. 10a and b, the concentration profiles across the interfaces of the $Ni_{16}Ti_6Si_7$- and $Ni_{16}Nb_6Si_7$-G phases are represented as proximity histograms. Additionally, Fig. 10c shows the averaged compositions of the precipitates and matrix. It is worth emphasizing that the $Ni_{16}Nb_6Si_7$_G phase contains ~20 at. % Fe in its core, while $Ni_{16}Ti_6Si_7$_G core exhibits almost no presence of Fe. This discrepancy indicates that even after a 12-h aging process, the $Ni_{16}Nb_6Si_7$_G phase remains a non-stoichiometric G-phase $(Fe, Ni)_{16}(Nb, Fe)_6Si_7$. Conversely, the $Ni_{16}Ti_6Si_7$_G phase achieves a composition that is very close to stoichiometric equilibrium following the same 12-h aging treatment. Thus, it is proposed that aging for 12 h is sufficient for the $Ni_{16}Ti_6Si_7$_G phase to reach equilibrium compositions through diffusion. The disparity in composition can be attributed to the slower diffusion of Nb compared to Ti.

The radius of the $Ni_{16}Ti_6Si_7$_G phase is slightly smaller than that of $Ni_{16}Nb_6Si_7$, as indicated in Fig. 10d. However, the number density of the $Ni_{16}Ti_6Si_7$_G phase is significantly higher than that of $Ni_{16}Nb_6Si_7$, approximately four times greater, as shown in Fig. 10e. In terms of volume fraction, the two phases are comparable, as depicted in Fig. 10f. Based on these findings, it can be speculated that the observed significant difference in aging hardness, as depicted in Fig. 5, may be primarily influenced by the number density of the precipitates.

5. Discussion

5.1. *Precipitation behavior of G-phase*

Considering phase stability, the dissolution temperatures of the $Ni_{16}Ti_6Si_7$, $Ni_{16}Ta_6Si_7$ and $Ni_{16}Nb_6Si_7$ can be anticipated to

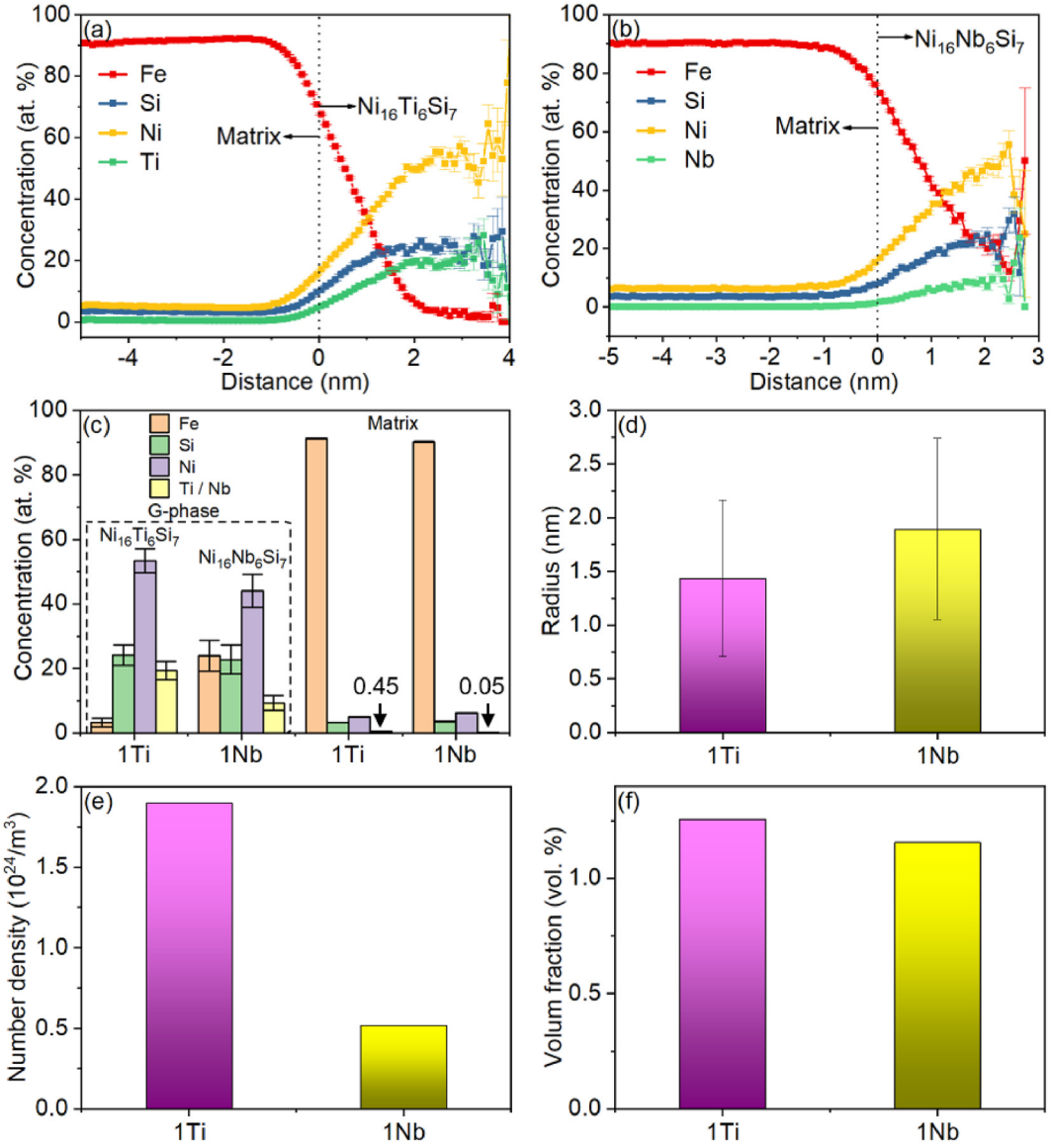

Fig. 10 – Quantitative statistics of precipitates ($Ni_{16}Ti_6Si_7$/$Ni_{16}Nb_6Si_7$) through APT characterization: (a) and (b) Composition profiles from matrix to the G-phase; (c) Particle radii, (d) Volume fraction, (e) Number density; (f) Averaged compositions of precipitate core and matrix.

fall within the medium temperature range of 600–700 °C as indicated by both our experimental findings (Figs. 6, 7 and 9) and theoretical results (Fig. 1a and b). Furthermore, these experimental observations also highlight the significantly high number density in 1Ti alloy is the primary reason for its exceptional hardness (refer to Fig. 10). Generally, the precipitation behavior is jointly determined by interfacial energy and strain energy. Our previously work has demonstrated that the difference in lattice misfit between the $Ni_{16}Ti_6Si_7$/α-Fe and $Ni_{16}Nb_6Si_7$/α-Fe is almost negligible [23,47]. Thus, it is plausible that their variations in interfacial energy contribute to the observed differences in number density. Our prior calculations have shown that the interfacial energy of $Ni_{16}Ti_6Si_7$/α-Fe is extremely low and the corresponding adhesive work is relatively high [48], which could partly support this speculation. Further calculations on the interfacial energies of $Ni_{16}Ta_6Si_7$/α-Fe and $Ni_{16}Nb_6Si_7$/α-Fe are warranted, even though they were not within the scope of this study.

And the $Ni_{16}Zr_6Si_7$- and $Ni_{16}Mn_6Si_7$-G phases exhibit distinct behaviors. The Fe-based thermodynamic database significantly underestimates the dissolution temperature of the $Ni_{16}Zr_6Si_7$-G phase (~840 °C, Fig. 1c) compared to the experimental value (>1000 °C, Fig. 2c and 3). Based on the morphology observed in Fig. 2c, which shows a dual-phase microstructure consisting of $Ni_{16}Zr_6Si_7$-G and α-Fe, it can be reasonably speculated that this morphology arises from the eutectic reaction of L → ($Ni_{16}Zr_6Si_7$-G + α-Fe) during solidification from the liquid phase [49]. An exciting opportunity exists to develop a G/α-Fe eutectic alloy with high strength through composition design and microstructural optimization. Moreover, it is important to note that there are two potential variants of the G-phase in the Fe–7Ni–2Si–1Zr quaternary alloy, namely $Fe_{16}Zr_6Si_7$ and $Ni_{16}Zr_6Si_7$ [50]. The dual-phase equilibrium involving $Ni_{16}Zr_6Si_7$-G and α-Fe has been experimentally confirmed only in the Fe–Zr–Si ternary system [51], and not in the Ni–Zr–Si system [52]. Therefore, it is reasonable to describe the detected G-phase in the Fe–7Ni–2Si–1Zr alloy as $(Fe, Ni)_{16}Zr_6Si_7$. Conversely, the $Ni_{16}Mn_6Si_7$-G phase exhibits low thermal stability within the expected aging temperature ranges. Our experimental results (Fig. 5) align precisely with the thermodynamic predictions (Fig. 1d), which collectively confirm the extremely low thermal stability of the $Ni_{16}Mn_6Si_7$-G phase. These experimental observations regarding the precipitation behavior of the G-phase are in strong agreement with the behavior observed in 20Cr ferritic stainless steel strengthened by the G-phase [25,50]. This similarity can be attributed to the comparable crystal structures of martensite and ferrite.

5.2. *Strengthening effect of G-phase*

The G-phase variants in maraging steel exhibit distinct precipitation behavior, leading to significant differences in their strengthening effects. After aging at 500 °C for 12 h, the 1Ti and 1Nb alloys demonstrated an estimated increase in microhardness of approximately 210 HV (equivalent to 693 MPa) and 135 HV (equivalent to 445 MPa), respectively (refer to Fig. 5). The enhanced hardness in the 1Ti alloy can be attributed to the precipitation of $Ni_{16}Ti_6Si_7$-G phases, which possess an average radius of approximately 1.4 nm, a number density of approximately $1.9 \times 10^{24}/m^3$, and a volume fraction of approximately 1.15 vol % (Fig. 10). Similarly, the increased hardness in the 1Nb alloy can be attributed to the precipitation of $Ni_{16}Nb_6Si_7$-G phases, which possess an average radius of ~2.0 nm, a number density of ~$4.9 \times 10^{23}/m^3$, and a volume fraction of approximately 1.19 vol %. Due to its inherent properties [47], the precipitate is assumed to be shear-resistant, and the deformation and strengthening are predominantly governed by the dislocation bypass mechanism [53]. The increase in yield strength ($\Delta\sigma_{or}$) resulting from the dislocation bypass mechanism can be calculated using Eqs. (1) and (2) as follows:

$$\Delta\sigma_{or} = \frac{0.4MGb}{\pi\sqrt{1-\vartheta}} \cdot \frac{\ln\left(\frac{2r}{b}\right)}{\lambda} \tag{1}$$

$$\lambda = \left(\sqrt{\frac{3\pi}{4f}} - 1.64\right) \cdot r \tag{2}$$

where M is the Taylor factor (=2.9) [54], b is the Burgers vector (=0.248 nm) [55], G is the shear modulus (=80 GPa) [56], ϑ is the Poisson ratio (=0.285) [57], f is the volume fraction of precipitate, r is the radius of precipitate, the effective inter-precipitate distance λ. Using Eqs. (1) and (2), the yield strength $\Delta\sigma_{or}$ can be estimated as ~ 1094 MPa and ~879 MPa for the 1Ti and 1Nb alloys, respectively.

Obviously, these calculated theoretical values are far greater than the measured value. This large difference between the theoretically calculated values and the measured values of yield strength in maraging steels can be attributed to the fact that multiple strengthening mechanisms are at play, not just precipitation strengthening. The aging process involves not only the precipitation of G-phase, but also other concurrent effects such as the reduction of solid solution elements, the increase in lath width, and the decrease in dislocation density. These factors can contribute to reducing the overall yield strength of the alloy. Assuming that the effects of reducing solid solution elements, increasing lath size, and decreasing dislocation density are similar for both the 1Nb and 1Ti alloys, the theoretically calculated difference in strengthening effect (215 MPa) between the two alloys is relatively close to the measured value (248 MPa). This suggests that the precipitation strengthening predominantly depends on the particle radius and volume fraction of the G-phase. As a result, the Ti-containing G-phase variant appears to be the preferred choice for strengthening maraging steel through the G-phase. These results indicate that the G-phase strengthened maraging steel designed with the Ti-containing variant still exhibits a high yield strength, highlighting its potential for practical applications.

6. Conclusions

In this study, the focus was on the alloy design and precipitation behavior of G-phase strengthened 7Ni maraging steels. The following conclusions were drawn.

(1) Four types of G-phases, specifically $Ni_{16}X_6Si_7$ (X = Ti, Nb, Ta, Zr), were successfully incorporated into the 7Ni

maraging steels through thermodynamic design with the exception of $Ni_{16}Mn_6Si_7$.

(2) Among the three G-phases, $Ni_{16}X_6Si_7$ (X = Ti, Nb, Ta), it was experimentally demonstrated that they effectively contributed to precipitation hardening within the 7Ni martensitic matrix. The Ti-containing alloy exhibited the highest aging hardness, reaching approximately 550 HV. This superior hardness was attributed to the presence of dense $Ni_{16}Ti_6Si_7$-G precipitates with an extremely high number density of ~$10^{24}/m^3$.

(3) The G-phases exhibited a strict cube-on-cube orientation relationship with the martensitic matrix, similar to their behavior in ferritic steels. This special orientation relationship further confirms the potential for effective strengthening in Fe-based martensitic alloy.

Overall, this study provides valuable insights into the precipitation behaviors of G-phase strengthened 7Ni maraging steels, paving the way for further advancements in the development of high-performance maraging steels.

Data availability statement

The raw/processed data required to reproduce these findings cannot be shared at this time as the data also forms part of an ongoing study.

Declaration of competing interest

The authors declare that they have no known competing financial interests or personal relationships that could have appeared to influence the work reported in this paper.

Acknowledgements

This work was financially funded by the Guangdong Provincial Basic and Applied Basic Research Fund Project-Regional Joint Fund-Youth Fund Project (Grant No. 2022A1515110279), the National Natural Science Foundation of China (Grant No. 52301153, 51971082), the Guangdong Provincial Department of Education University Youth Innovative Talent Research Project (Grant No. 2022KQNCX068) and the Key-Area Research Project of the Guangdong Province Department of Education (No. 2022ZDZX3021). All authors gratefully acknowledge the assistance of Dr. Yang Qiu and Dr. Dongsheng He at SUStech Core Research Facilities.

REFERENCES

[1] Jiang S, Wang H, Wu Y, Liu X, Chen H, Yao M, et al. Ultrastrong steel via minimal lattice misfit and high-density nanoprecipitation. Nature 2017;544(7651):460–4.

[2] Jiao ZB, Luan JH, Miller MK, Liu CT. Precipitation mechanism and mechanical properties of an ultra-high strength steel hardened by nanoscale NiAl and Cu particles. Acta Mater 2015;97:58–67.

[3] Jiao Z, Luan J, Miller M, Chung Y, Liu CJMT. Co-precipitation of nanoscale particles in steels with ultra-high strength for a new era 2017;20(3):142–54.

[4] Jiao Z, Luan J, Zhang Z, Miller MK, Ma W, Liu CJAm. Synergistic effects of Cu and Ni on nanoscale precipitation and mechanical properties of high-strength steels 2013;61(16):5996–6005.

[5] Li Y, Yan W, Cotton JD, Ryan GJ, Shen Y, Wang W, et al. Design, A new 1.9 GPa maraging stainless steel strengthened by multiple. precipitating species 2015;82:56–63.

[6] Pereloma EV, Shekhter A, Miller MK, Ringer SPJAM. Ageing behaviour of an Fe–20Ni–1.8 Mn–1.6 Ti–0.59 Al (wt%) maraging alloy: clustering, precipitation and hardening 2004;52(19):5589–602.

[7] Sun W, Marceau R, Styles M, Barbier D, Hutchinson CJAM. G phase precipitation and strengthening in ultra-high strength ferritic steels: towards lean 'maraging'metallurgy 2017;130:28–46.

[8] Zhou B, Yang T, Zhou G, Wang H, Luan J, Jiao ZJAM. Mechanisms for suppressing discontinuous precipitation and improving mechanical properties of NiAl-strengthened steels through nanoscale. Cu partitioning 2021;205:116561.

[9] Simm T, Sun L, Galvin D, Gilbert E, Venero DA, Li Y, et al. A SANS and APT study of precipitate evolution and strengthening in a maraging steel 2017;702:414–24.

[10] Niu M, Yin L, Yang K, Luan J, Wang W, Jiao ZJAM. Synergistic alloying effects on nanoscale precipitation and mechanical properties of ultrahigh-strength steels strengthened by Ni3Ti, Mo-enriched. and Cr-rich co-precipitates 2021;209:116788.

[11] Niu M, Zhou G, Wang W, Shahzad MB, Shan Y, Yang KJAM. Precipitate evolution and strengthening behavior during aging process in a 2. 5 GPa grade maraging steel 2019;179:296–307.

[12] Jiao Z, Liu C-TJSB. Ultrahigh-strength steels strengthened by nanoparticles 2017;62(15):1043–4.

[13] Isheim D, Gagliano MS, Fine ME, Seidman DN. Interfacial segregation at Cu-rich precipitates in a high-strength low-carbon steel studied on a sub-nanometer scale. Acta Mater 2006;54(3):841–9.

[14] Wen Y, Hirata A, Zhang Z, Fujita T, Liu C, Jiang J, et al. Microstructure characterization of Cu-rich nanoprecipitates in a Fe–2.5 Cu–1.5 Mn–4.0 Ni–1.0 Al multicomponent ferritic alloy 2013;61(6):2133–47.

[15] Wei X, Cao X, Luan J, Jiao Z, Liu C, Zhang ZJMS, et al. Synergy of strengthening and toughening of a Cu-rich precipitate-strengthened steel. 2021. p. 142487.

[16] Haase C, Zehnder C, Ingendahl T, Bikar A, Tang F, Hallstedt B, et al. On the deformation behavior of κ-carbide-free and κ-carbide-containing high-Mn. light-weight steel 2017;122:332–43.

[17] Brasche F, Haase C, Lipińska-Chwałek M, Mayer J, Molodov DAJMS, A E. Combined κ-carbide precipitation and recovery enables ultra-high strength and ductility in light-weight steels, 795; 2020. p. 139928.

[18] Moon J, Park S-J, Jang JH, Lee T-H, Lee C-H, Hong H-U, et al. Atomistic investigations of κ-carbide precipitation in austenitic Fe-Mn-Al-C lightweight steels and the effect of Mo addition 2017;127:97–101.

[19] Song G, Sun Z, Li L, Xu X, Rawlings M, Liebscher CH, et al. Ferritic alloys with extreme creep resistance via coherent hierarchical precipitates 2015;5(1):1–14.

[20] Rawlings MJ, Liebscher CH, Asta M, Dunand DCJAM. Effect of titanium additions upon microstructure and properties of precipitation-strengthened Fe-Ni-Al-Cr. ferritic alloys 2017;128:103–12.

[21] Baik S-I, Wang S-Y, Liaw PK, Dunand DCJAM. Increasing the creep resistance of Fe-Ni-Al-Cr superalloys via Ti additions

by optimizing the B2/L21 ratio in composite nano-precipitates 2018;157:142–54.
[22] Chen W-Y, Li M, Zhang X, Kirk MA, Baldo PM, Lian TJJoNM. In situ TEM study of G-phase precipitates under heavy ion irradiation in CF8 cast austenitic stainless steel 2015;464:185–92.
[23] King D, Yang M, Whiting T, Liu X, Wenman M. G-phase strengthened iron alloys by design. Acta Mater 2020;183:350–61.
[24] Matsukawa Y, Takeuchi T, Kakubo Y, Suzudo T, Watanabe H, Abe H, et al. The two-step nucleation of G-phase in ferrite. Acta Mater 2016;116:104–13.
[25] Yang M, King DJ, Povstugar I, Wen Y, Luan J, Kuhn B, et al. Precipitation behavior in G-phase strengthened ferritic stainless steels, 205; 2021. p. 116542.
[26] King D, Yang M, Whiting T, Liu X, Wenman MJAM. G-phase strengthened iron alloys by design 2020;183:350–61.
[27] Yan X, Grytsiv A, Rogl P, Pomjakushin V, Xue XJJoa. compounds, on the crystal structure of the Mn–Ni–Si. G-phase 2009;469(1–2):152–5.
[28] King D, Burr P, Middleburgh S, Whiting T, Burke M, Wenman MJJoNM. The formation and structure of Fe-Mn-Ni-Si solute clusters and G-phase precipitates in steels 2018;505:1–6.
[29] Yang M, Zhu J, Yang T, Luan J, Jiao Z, Fan X, et al. A novel ferritic steel family hardened by intermetallic compound. G-phase 2019;745:390–9.
[30] Keimes V, Mewis A. Mg6Ni16As7-eine neue G-phase/Mg6Ni16As7-a new G phase. 2014.
[31] Mateo A, Llanes L, Anglada M, Redjaimia A, Metauer G. Characterization of the intermetallic G-phase in an AISI 329 duplex stainless steel. J Mater Sci 1997;32(17):4533–40.
[32] Ecob R, Lobb R, Kohler V. The formation of G-phase in 20/25 Nb stainless steel AGR fuel cladding alloy and its effect on creep properties. J Mater Sci 1987;22(8):2867–80.
[33] Pareige C, Emo J, Saillet S, Domain C, Pareige P. Kinetics of G-phase precipitation and spinodal decomposition in very long aged ferrite of a Mo-free duplex stainless steel. J Nucl Mater 2015;465:383–9.
[34] Shuro I, Kuo H, Sasaki T, Hono K, Todaka Y, Umemoto MJMS, et al. G-phase precipitation in austenitic stainless steel deformed by high pressure torsion 2012;552:194–8.
[35] Beattie H, Versnyder FJN. A new complex phase in a high-temperature alloy 1956;178(4526):208–9.
[36] Sunil S, Kapoor R, Sarkar S, Biswas A, Donthula H, Sen DJAM. Ultra-high strength steel made from AISI 304L using a novel thermo-mechanical processing technique 2021;221:117379.
[37] Schulz-Beeker A, Hougardy S,H. P. % J developement of high-strength martensite by age-hardening of coherent intermetallic precipitates. European Symposium on Martensitic Transformations 1989:473–80.
[38] Gemperle A, Gemperlova J, Sha W, Smith GJMs. Technology, Aging behaviour of cobalt free chromium containing maraging steels 1992;8(6):546–54.
[39] Chen Y, Dai X, Chen X, Yang BJMC. The characterization of G-phase in Fe20Cr9Ni cast duplex stainless steel 2019;149:74–81.
[40] Pareige C, Emo J, Saillet S, Domain C, Pareige PJJoNM. Kinetics of G-phase precipitation and spinodal decomposition in very long aged ferrite of a Mo-free duplex stainless steel 2015;465:383–9.
[41] Hamaoka T, Nomoto A, Nishida K, Dohi K, Soneda NJPM. Effects of aging temperature on G-phase precipitation and ferrite-phase decomposition in duplex stainless steel 2012;92(34):4354–75.
[42] Li S, Wang Y, Wang X, Xue F. G-phase precipitation in duplex stainless steels after long-term thermal aging: a high-resolution transmission electron microscopy study. J Nucl Mater 2014;452(1–3):382–8.
[43] Liu X, Liu C, Wu J, Zhang X, Zhu X, Wang JJMS, et al. Morphological instability of the G-phase induced a different contribution to hardening of ferrite phase in a duplex stainless steel 2022;832:142421.
[44] Wang C, Huang L, Yang M, Huang X, Zhang J, Pan S, et al. Compounds, Experimental investigation of phase equilibria in the Ni-Ta-Si refractory. alloy system 2021;888:161467.
[45] Xingjun L, Cui Y, Huang L, Yang M, Yang F, Zhang J, et al. Experimental investigation and thermodynamic calculation of phase equilibria in the ternary Fe-Si-Ta system. J Alloys Compd 2023:170741.
[46] Miller MK, Russell KF. Atom probe specimen preparation with a dual beam SEM/FIB miller. Ultramicroscopy 2007;107(9):761–6.
[47] Wang C, Huang X, Yang M, Han J, Yao Z, Yang T, et al. Development of novel ferritic steels strengthened by the Co16X6Si7-G phase: a theoretical and experimental study. Mater Des 2022;222:111021.
[48] Yang M, Huang C, Han J, Wu H, Zhao Y, Yang T, et al. Development of the high-strength ductile ferritic alloys via regulating the intragranular and grain boundary precipitation of G-phase. J Mater Sci Technol 2023;136:180–99.
[49] Tiwary CS, Pandey P, Sarkar S, Das R, Samal S, Biswas K, et al. Five decades of research on the development of eutectic as engineering materials. Prog Mater Sci 2022;123:100793.
[50] Yang M, Zhu J, Yang T, Luan J, Jiao Z, Fan X, et al. A novel ferritic steel family hardened by intermetallic compound G-phase. Mater Sci Eng, A 2019;745:390–9.
[51] Wang CP, Hu Y, Yang SY, Lu Y, Jiang QW, Liu XJ. Experimental investigation of phase equilibria in the Fe-Si-Zr ternary system. J Phase Equilibria Diffus 2013;34(4):277–88.
[52] Locci IE, Dickerson RM, Garg A, Noebe RD, Whittenberger JD, Nathal MV, et al. Microstructure and phase stability of single crystal NiAl alloyed with Hf and Zr. J Mater Res 1996;11(12):3024–38.
[53] Orowan E. Fracture and strength of solids. Rep Prog Phys 1949;12(1):185.
[54] Rosenberg J, Piehler H. Calculation of the Taylor factor and lattice rotations for bcc metals deforming by pencil glide. Metall Trans A 1971;2:257–9.
[55] Marukawa K, Kajiwara S. On the Burgers vector of dislocations produced by a cyclic bcc/9R martensitic transformation. Philos Mag A 1987;55(1):85–97.
[56] Gladman T. Precipitation hardening in metals. Mater Sci Technol 1999;15(1):30–6.
[57] Krenn C, Roundy D, Morris Jr J, Cohen ML. Ideal strengths of bcc metals. Mater Sci Eng, A 2001;319:111–4.